PERGAMON

International Journal of Multiphase Flow 27 (2001) 1555–1577

International Journal of Multiphase Flow

www.elsevier.com/locate/ijmulflow

# Wave- and turbulence-induced secondary currents in the liquid phase in stratified duct flow

M. Nordsveen

*Studsvik Scandpower AS, P.O. Box 15, Kjeller 2027, Norway*

Received 23 December 1999; received in revised form 30 January 2001

**Abstract**

Turbulent gas–liquid stratified flow in near-horizontal, straight ducts with a regular two-dimensional wavy deformation of the interface has been studied. In this flow regime strong mean secondary currents have been observed. It was previously shown that these secondary velocities in the liquid phase may result from an interaction between wave pseudomomentum and mean axial velocity. In the present work also a model for turbulence-induced secondary flows due to anisotropy in the Reynolds stresses has been considered. For a wide duct case it was seen that the wave field model generated larger secondary flows than the ones induced by the turbulence model. However, the best agreement with the experimental results was obtained when the two effects were combined. For a more narrow duct the models indicated that waves and turbulence can be of equal importance in inducing secondary currents. 

*Keywords:* Duct flow; Secondary currents; Regular waves; Wave pseudomomentum; Anistropic turbulence; ASM-model

## 1. Introduction

When gas and liquid flow co-currently through a horizontal duct, stratified flow occurs at fairly low flow rates with the heavier liquid flowing along the bottom of the duct with the gas above the liquid. This regime has been studied by several researchers and it can be divided into two main subregimes; the stratified smooth and the stratified wavy regime. In the wavy regime the interface between the liquid and the gas is characterized by complicated wave patterns and several new subregimes have been introduced according to the wave structure. Hanratty and Engen (1957), Akai et al. (1977), Suzanne (1985) and others have identified a subregime with quite regular deformation of the interface with two-dimensional waves or three-dimensional "pebbled" structures. Together with this regular wave field, Suzanne (1985) observed a strong mean secondary flow, which formed a cellular structure with two rolls in the liquid phase and two rolls in the gas

0301-9322/01/$ - see front matter 
PII: S0301-9322(01)00015-5

phase. The liquid was flowing up near the walls and down in the middle of the duct, while the gas was flowing up in the middle and down near the walls. The flow field was fully turbulent in both the gas and the liquid phase. Suzanne conducted his experiments in a duct with rectangular cross-section. However, in a similar investigation, Strand (1993) observed the regular wave regime with transverse secondary flows also in a circular pipe.

For the stratified smooth regime, Suzanne found no secondary currents in the liquid in the middle of the duct (liquid width to height aspect ratio of about five). This indicates that the strong secondary currents in the presence of waves are caused by the wave field. However, also turbulence is known to generate secondary currents. Nikuradse (1926) measured mean axial velocity distributions in turbulent flow through several closed geometries as well as an open rectangular channel. He observed that in geometries with non-circular cross-section, lines of constant axial velocity are displaced more towards the corners than for a similar laminar flow. Prandtl (1926) suggested that the bending of the velocity contours was caused by turbulent generated mean secondary flow towards the corners. Einstein and Li (1958) showed theoretically, for single phase turbulent flow in a straight conduit, that anisotropy in the turbulent Reynolds stresses can introduce axial mean vorticity (secondary currents) by

$$\mathbf{S}'_{\Omega} = \left[ \underbrace{\frac{\partial^2}{\partial x \partial y}\left(\overline{u'u'} - \overline{v'v'}\right)}_{S'_{\Omega 1}} - \underbrace{\left(\frac{\partial^2}{\partial x^2} - \frac{\partial^2}{\partial y^2}\right)\overline{u'v'}}_{S'_{\Omega 2}} \right] \mathbf{i}_z, \tag{1}$$

where $\overline{u'u'}$, $\overline{v'v'}$ and $\overline{u'v'}$ denote turbulent Reynolds stresses per mass in the cross section. $\mathbf{i}_z$ is the axial unit vector, $x$ is the horizontal, transversal coordinate and $y$ is the vertical coordinate. Brundrett and Baines (1964) measured all Reynolds stresses in turbulent flow in a horizontal square duct and deduced that differences in normal stresses ($S'_{\Omega 1}$) are necessary to initiate axial mean vorticity. Perkins (1970) conducted experiments for developing flow near one corner of a square duct and found that the terms $S'_{\Omega 1}$ and $S'_{\Omega 2}$ were of equal importance and interpreted the $S'_{\Omega 1}$ term as a generating term and the $S'_{\Omega 2}$ term as a transport (diffusive) term. This was confirmed by Huser (1992) who performed direct numerical simulations (DNS) of Navier–Stokes equation in a squared duct. Naot and Rodi (1982) applied an algebraic Reynolds stress (ASM) model to predict turbulence generated secondary currents in open channel flow with a free surface not disturbed by waves, and Nezu and Rodi (1985) measured secondary velocities in open channel flow and related these flows to the turbulence. In Naot and Rodi's computations and in the measurements of Nezu and Rodi, the secondary velocities attain their largest values close to the lateral walls with relatively small values, a few liquid heights away from the lateral walls. This is in agreement with Suzanne's (1985) findings of zero secondary flows in the middle of a relatively wide duct for smooth stratified flow.

When reviewing wave-induced 'cross-flow' currents, Langmuir circulation occurring in lakes and oceans is of interest. When wind blows over the water surface and generates waves, numerous streaks parallel to the wind direction may be observed. Langmuir (1938) discovered that the streaks were convergence lines between counter rotating vortices below the surface. Craik and Leibovich (1976), Craik (1977) and Leibovich (1977) presented models (denoted CL1 and CL2, respectively) where the vortices are induced by interactions between Stokes drift due to the wave

field and a weak shear flow induced by the wind. The two CL mechanisms can be discussed in terms of "vortex forces" (Leibovich, 1983) in the vorticity equation given by

$$\tilde{\mathbf{S}}_{\mathrm{CL}} = (\underbrace{\overline{w}^S_{,x} W_{,y}}_{\tilde{S}_{\mathrm{CL1}}} - \underbrace{\overline{w}^S_{,y} W_{,x}}_{\tilde{S}_{\mathrm{CL2}}})\mathbf{i}_z, \tag{2}$$

where $\overline{w}^S$ and $W$ denote the Stokes drift and mean velocity in the wind direction $z$, respectively. Subscripts $,x$ and $,y$ mean differentiation with respect to $x$ and $y$. In the CL1 model a non-zero $\tilde{S}_{\mathrm{CL1}}$ term is produced by an interaction between the mean shear flow's vertical variation and horizontal ($x$-direction) variation of the Stokes drift. In the CL2 model a non-zero $\tilde{S}_{\mathrm{CL2}}$ term is produced by an interaction between the mean shear flow's horizontal variation ($x$-direction) and the vertical variation of the Stokes drift.

An important difference between flow in the ocean and in ducts is the relative magnitude between the mean shear flow and the wave perturbation. In the ocean, the wind-induced shear stress is weak and the wave field in the CL models is regarded as irrotational. In duct flow, there is a strong shear flow and the wave field is not essentially irrotational. Nevertheless, Benkirane et al. (1990) applied a CL2 model for the liquid phase in duct flow and obtained secondary velocities which agreed fairly well with Suzanne's (1985) measurements.

Nordsveen and Bertelsen (1996) developed a model for the liquid phase in duct flow with a wave field composed of two crossing linear wave trains interacting with a strong mean flow giving a rotational wave solution. Reynolds averaging with a decomposition of the flow field into a mean, a wave and a turbulent component was applied. This gave a mean momentum equation with a turbulent Reynolds stress term and a wave Reynolds stress term. Mean secondary currents were induced by the wave field through the wave Reynolds stress term. However, the secondary currents were small compared with Suzanne's (1985) measurements.

By applying the generalized Lagrangian mean (GLM) theory of Andrews and McIntyre (1978), Nordsveen and Bertelsen (1997) showed that secondary velocities in the liquid phase may result from an interaction between wave pseudomomentum per unit mass and mean axial velocity. This interaction takes the same form as the Craik and Leibovich "vortex forces" but with wave pseudomomentum per unit mass $P_z$ replacing Stokes drift:

$$\tilde{\mathbf{S}}_{\Omega} = (\underbrace{P_{z,x} W_{,y}}_{\tilde{S}_{\Omega 1}} - \underbrace{P_{z,y} W_{,x}}_{\tilde{S}_{\Omega 2}})\mathbf{i}_z. \tag{3}$$

This is a more general expression since the assumption of a weak shear flow is not invoked and interactions between a strong shear flow and waves entailing a rotational wave field are included. A sketch of the two mechanisms is shown in Fig. 1. The variation of the wave pseudomomentum across the duct interacts with the vertical variation of the axial velocity giving the $\tilde{S}_{\Omega 1}$ term. The variation with depth of the wave pseudomomentum interacts with the variation of the axial velocity across the duct giving the $\tilde{S}_{\Omega 2}$ term. Both the axial velocity and the wave field decrease with depth in duct flow. The axial velocity varies laterally, going to zero at the walls, and a lateral variation of wave pseudomomentum is present due to a varying wave field amplitude, as measured by Suzanne (1985). Magnaudet (1989) and Line et al. (1996) showed that such an amplitude variation can be caused by the existence of a caustic between the lateral wall and the center of the duct. Thus all the necessary gradients to obtain non-zero $\tilde{S}_{\Omega 1}$ and $\tilde{S}_{\Omega 2}$ seem to be present in wavy

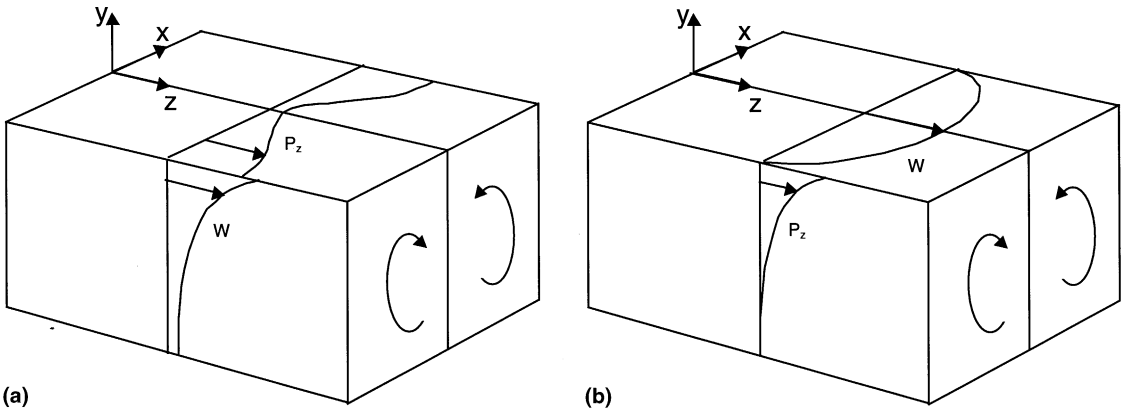


Fig. 1. A sketch of the quantities involved in the wave pseudomomentum – shear flow vortex forces: (a) $\tilde{S}_{\Omega 1}$; (b) $\tilde{S}_{\Omega 2}$.

stratified duct flow. In the model by Nordsveen and Bertelsen (1997) the interaction between wave pseudomomentum and the strong shear flow in ducts gave secondary velocities which agreed fairly well with Suzanne's (1985) measurements. $\tilde{S}_{\Omega 2}$ was found to be one order of magnitude larger than $\tilde{S}_{\Omega 1}$ for this case and was the principal source for the secondary currents. Interesting is that the curl of the wave Reynolds stress term used in the work by Nordsveen and Bertelsen (1996) was identical to $\tilde{S}_{\Omega 1}$ invoking their wave field model. This explains why the Nordsveen and Bertelsen (1996) model gave too small secondary flows.

For the strong shear flow and rotational wave field, Nordsveen and Bertelsen (1997) found that generalized Stokes drift and wave pseudomomentum per mass are significantly different. This is in contrast to the irrotational wave field case used in the CL theories (see above) for which Andrews and McIntyre (1978) showed that wave pseudomomentum per mass is to a leading order equal to the Stokes drift. Nordsveen and Bertelsen (1997) found that wave pseudomomentum for the irrotational and rotational wave fields was very similar and that it was the Stokes drift which was changed considerably. This entails that the wave pseudomomentum secondary flow sources used by Nordsveen and Bertelsen (1997) for a strong shear flow are similar to the CL – Stokes drift secondary flow sources for a weak shear flow.

In the present work, both wave and turbulence-induced secondary currents are considered. In the previous works mentioned above, Benkirane et al. (1990) and Nordsveen and Bertelsen (1997) modelled wave field-induced secondary currents with fairly good agreement with the measurements by Suzanne (1985). However, there were some discrepancies between predicted and measured secondary currents and particularly so close to the lateral walls. We believed this could be due to the neglect of turbulence-induced secondary flow and this initiated the present work where the ASM model of Naot and Rodi (1982) has been incorporated in the previous model of Nordsveen and Bertelsen (1997). Simulations with only turbulence-induced secondary flows, with only wave-induced secondary flows and with combined wave- and turbulence-induced secondary flows are performed.

The Naot and Rodi (1982) model was developed for open channel flow not disturbed by waves and direct interactions between waves and turbulence have not been taken into account. This has

been addressed in other studies and we refer to the work by Magnaudet (1989) who analyzed wavy stratified duct flow and the interactions between waves and turbulence.

## 2. Mathematical models

A sketch of the flow problem is given in Fig. 2. A Cartesian coordinate system $(x, y, z)$ is used, where for a horizontal duct, $x$ is the horizontal, spanwise direction, $y$ is the vertical direction and $z$ is the axial direction. The inclination angle of the duct is denoted $\gamma$. The bottom of the duct, the mean liquid height and the lateral walls are given by $y = 0$, $y = H_L$ and $x = \pm L_W$, respectively. The liquid flow is assumed incompressible and Newtonian under the influence of a constant gravitational field. $\mathbf{v} = (u, v, w)$ and $p$ denote the velocity and pressure field, respectively. The flow is turbulent and the interface between the liquid and the gas is assumed to be deformed by linear harmonic two-dimensional waves. The interface deviation $\eta$ is modelled as

$$\eta = 2a \sin[k_w(z - ct)], \tag{4}$$

where $2a$ is the amplitude of the waves, $k_w$ is the wave number, $c$ is the wave speed and $t$ is time. This gives a wave field with a constant wave amplitude across the width of the duct.

Suzanne (1985) measured a varying wave amplitude with about a doubling from the middle of the duct towards the lateral walls. Magnaudet (1989) and Line et al. (1996) showed that this amplitude variation can be caused by the existence of a caustic between the lateral wall and the center of the duct. There is no attempt to model this in the present work. Nordsveen and Bertelsen (1997) applied both a constant wave amplitude and a cross-stream varying amplitude which was the result of two crossing wave trains propagating with equal and opposite angle to the axial direction. The crossing waves gave zero amplitude in the middle of the duct and thus overestimated the lateral variation and the authors reported the best agreement with Suzanne's (1985) secondary flow measurements with the constant wave amplitude model, Eq. (4).

The waves are approximately linear when

$$\epsilon_1 = \max(2a/\lambda, 2a/H_L) \ll 1, \tag{5}$$

where $\lambda$ is the length of the waves. The mean secondary velocities are small compared with the mean axial velocity. This entails that

$$\epsilon_2 = \max(U/W_B, V/W_B) \ll 1, \tag{6}$$

where $U$, $V$ denote the mean velocity components in the $x$- and $y$-directions, respectively, and $W_B$ is the bulk velocity.

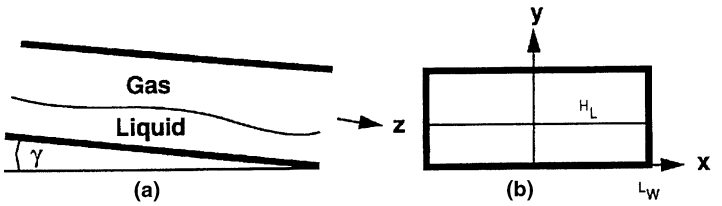


Fig. 2. A sketch of the duct flow problem: (a) axial cut; (b) cross-section.

Time and phase averages of a field quantity $f(\mathbf{x},t)$ are defined by (Reynolds and Hussain, 1972)

$$\overline{f}(\mathbf{x}) = \lim_{T\to\infty}\frac{1}{T}\int_0^T f(\mathbf{x},t)\,\mathrm{d}t, \tag{7}$$

$$\langle f(\mathbf{x},t)\rangle = \lim_{N\to\infty}\frac{1}{N+1}\sum_{n=0}^{N} f(\mathbf{x},t+n\tau), \tag{8}$$

respectively, where $\tau$ is the period of the regular wave component. By applying these averages the flow field, $f$ is decomposed as $f = F + \tilde{f} + f'$, where $F = \overline{f}$ is the mean component, $\tilde{f} = \langle f\rangle - F$ is the wave component and $f' = f - \langle f\rangle$ is the turbulent component.

### 2.1. Equations for the mean field

The GLM theory of Andrews and McIntyre (1978) was used by Nordsveen and Bertelsen (1997) to develop an equation for the Lagrangian velocity field, which subsequently was transformed to an equation for the Eulerean velocity field. The Navier–Stokes equations for incompressible flow were first phase averaged and the GLM theory was applied to the phase averaged field. A Lagrangian mean operator $\overline{(\,)}^{\mathrm{L}}$ defined by

$$\overline{f(\mathbf{x},t)}^{\mathrm{L}} \equiv \overline{\langle f(\mathbf{x}+\boldsymbol{\xi}(\mathbf{x},t),t)\rangle}, \tag{9}$$

where $\overline{(\,)}$ in the present case is the time average, Eq. (7) was used. $\boldsymbol{\xi}(\mathbf{x},t)$ is the displacement due to the regular wave field about position $\mathbf{x}$. The wave pseudomomentum per unit mass $\mathbf{P}$ is given by

$$\mathbf{P} = (P_x,P_y,P_z) = -\overline{\nabla\boldsymbol{\xi}\cdot\mathbf{v}^l}, \tag{10}$$

where $\mathbf{v}^l$ is the fluctuating part of the Lagrangian velocity field defined as $\mathbf{v}^l \equiv \langle\mathbf{v}(\mathbf{x}+\boldsymbol{\xi}(\mathbf{x},t),t)\rangle - \overline{\mathbf{v}}^{\mathrm{L}}$, which for small amplitude waves can be expressed as $\mathbf{v}^l = \tilde{\mathbf{v}} + \boldsymbol{\xi}\cdot\nabla\mathbf{V} + O(\epsilon_1^2)$. The Eulerean mean momentum equations developed by Nordsveen and Bertelsen (1997) read:

$$\nabla\cdot(\mathbf{V}\mathbf{V}) = -\nabla\pi - \nabla\cdot\overline{\mathbf{v}'\mathbf{v}'} + P_z W_{,y}\mathbf{i}_y + P_z W_{,x}\mathbf{i}_x, \tag{11}$$

where $\pi = \overline{p}^{\mathrm{L}}/\rho + \overline{\Phi}^{\mathrm{L}} - \overline{\tilde{\mathbf{v}}\cdot\tilde{\mathbf{v}}}/2$. $\rho$ is the density and $\phi$ is the potential due to the gravity field. $\mathbf{v}'$ and $\tilde{\mathbf{v}}$ are the turbulent and wave velocity fields, respectively, and $W$ is the axial component of the mean velocity field $\mathbf{V}$. In developing the present form of the mean momentum equations, linear waves were assumed and interactions between waves and turbulence were disregarded. Interactions between the wave field and the mean secondary velocities were also disregarded since the secondary velocities are much smaller than the axial velocity. The fact that wave pseudomomentum and Stokes drift have mainly non-zero components in the axial direction was also utilized. Molecular viscosity terms are also disregarded in solving the equations in the fully turbulent region only, with 'laws of the wall' as boundary conditions.

By applying the curl operator on Eq. (11), the vorticity equation with the axial vorticity sources discussed in the introduction is obtained:

$$\nabla\times\nabla\cdot(\mathbf{V}\mathbf{V}) = -\nabla\times\nabla\cdot\overline{\mathbf{v}'\mathbf{v}'} + (\underbrace{P_{z,x}W_{,y}}_{\tilde{S}_{\Omega 1}} - \underbrace{P_{z,y}W_{,x}}_{\tilde{S}_{\Omega 2}})\mathbf{i}_z. \tag{12}$$

The mean flow field has to fulfill the continuity equation

$$\nabla \cdot \mathbf{V} = 0. \tag{13}$$

### 2.2. Equation for the wave field

The momentum equations for the wave field, also used by Nordsveen and Bertelsen (1996, 1997), are obtained as the difference between the phase averaged (8) and the time averaged (7) Navier–Stokes equations (see Reynolds and Hussain, 1972). These equations are simplified, applying an order-of-magnitude analysis considering that $W \sim W_B$, $U \sim V \ll W_B$ and $\tilde{\mathbf{v}} \ll W_B$. Molecular viscosity effects, as well as the difference between the phase averaged and time averaged turbulent Reynolds stress tensors, are neglected. In addition the variation in the mean axial velocity across the width of the duct is not taken into account. This last simplification is not valid close to the lateral walls. The momentum equations for the wave field read

$$\tilde{\mathbf{v}}_{,t} + \widehat{W} \cdot \nabla \tilde{\mathbf{v}} + \tilde{v} \widehat{W}_{,y} \mathbf{i}_z = -\frac{1}{\rho} \nabla \tilde{p}, \tag{14}$$

where

$$\widehat{W}(y) = \frac{1}{2L_w} \int_{-L_w}^{L_w} W(x,y)\, \mathrm{d}x$$

is the average of the axial mean velocity over the width of the duct.

The wave flow field has to fulfill the continuity equation

$$\nabla \cdot \tilde{v} = 0. \tag{15}$$

A solution of the above momentum and continuity equations subject to the interface deformation is given by

$$\tilde{u} = 0, \tag{16}$$

$$\tilde{v} = \phi(y) \cos[k_w(z - ct)], \tag{17}$$

$$\tilde{w} = -\frac{\phi_{,y}(y)}{k_w} \sin[k_w(z - ct)], \tag{18}$$

where $\phi(y)$ is the solution of Rayleigh's stability equation

$$(\widehat{W} - c)(\phi_{,yy} - k_w^2 \phi) - \phi \widehat{W}_{,yy} = 0. \tag{19}$$

The corresponding displacement field, given by Craik (1982), reads

$$\xi_x = 0, \tag{20}$$

$$\xi_y = \frac{\phi(y)}{k_w(\widehat{W} - c)} \sin[k_w(z - ct)], \tag{21}$$

$$\xi_z = -\left( \frac{\widehat{W}_{,y}\phi(y)}{k_w(\widehat{W} - c)} - \frac{\phi_{,y}(y)}{k_w} \right) \frac{1}{k_w(\widehat{W} - c)} \cos[k_w(z - ct)]. \tag{22}$$

### 2.3. Equations for the turbulent field

Both a $k-\epsilon$ model and an ASM model have been used. The $k-\epsilon$ model is applied, when only wave-induced secondary currents are considered. The ASM model is applied when turbulence-induced secondary currents are considered.

#### 2.3.1. $k-\epsilon$ model

When using the $k-\epsilon$ turbulence model, the Reynolds stresses per unit mass are described with the generalized Boussinesq hypothesis:

$$-\overline{\mathbf{v}'\mathbf{v}'} = \nu_t(\nabla\mathbf{V} + \nabla\mathbf{V}^T) - \frac{2}{3}k\mathscr{I}, \tag{23}$$

where $\mathscr{I}$ is the unit tensor, $k$ is the turbulent kinetic energy per unit mass and $\nu_t$ is the eddy viscosity modelled by the $k-\epsilon$ turbulence model $\nu_t = c_\mu k^2/\epsilon$, where $\epsilon$ is the dissipation rate of $k$. We adopt the transport equations for $k$ and $\epsilon$ as given by Rodi (1980)

$$\mathbf{V}\cdot\nabla k = \nabla\cdot\left(\frac{\nu_t}{\sigma_k}\nabla k\right) + \underbrace{\nu_t(\nabla\mathbf{V} + \nabla\mathbf{V}^T):\nabla\mathbf{V}}_{P_k} - \epsilon, \tag{24}$$

$$\mathbf{V}\cdot\nabla\epsilon = \nabla\cdot\left(\frac{\nu_t}{\sigma_\epsilon}\nabla\epsilon\right) + \frac{\epsilon}{k}(c_{1\epsilon}P_k - c_{2\epsilon}\epsilon). \tag{25}$$

The constants in the turbulence model are given in Table 1.

#### 2.3.2. ASM model

The algebraic stress model (ASM) due to Naot and Rodi (1982) has been applied. The expressions for the stresses are obtained by simplifying the Reynolds stress equations of Launder et al. (1975). Both convective and diffusive transport of Reynolds stresses are neglected. The Reynolds stresses per unit mass in the axial momentum equation are given by

$$\overline{u'w'} = -\nu_{tx}W_{,x}, \tag{26}$$

$$\overline{v'w'} = -\nu_{ty}W_{,y}, \tag{27}$$

where

$$\nu_{tx} = \left[\frac{c_1 + 2.5c_3f_2}{c_1 + 2c_3f_2}\right]c_\mu\frac{k^2}{\epsilon}, \tag{28}$$

$$\nu_{ty} = \left[\left(\frac{c_1}{c_1 + 1.5c_3f_2}\right)\left(\frac{c_1}{c_1 + 2c_3f_2}\right)\right]c_\mu\frac{k^2}{\epsilon}. \tag{29}$$

Table 1
Constants in $k-\epsilon$ turbulence model

| | | | | |
|---|---|---|---|---|
| $c_\mu = 0.09$ | $\sigma_k = 1.0$ | $\sigma_\epsilon = 1.3$ | $c_{1\epsilon} = 1.44$ | $c_{2\epsilon} = 1.92$ |

The $f_2$-function, given by Eq. (A.7) in Appendix A, is a free surface modification function. For closed ducts this term is neglected and the standard $k-\epsilon$ model for eddy viscosity is obtained for the stresses in the axial momentum equation. Other functions in the above stresses are given in Table 2.

The $f_1$-term, given by Eq. (A.1) in Appendix A, is a near-wall modification term which is a function of the integrated distance from all surrounding walls. The Reynolds stresses in the cross-section momentum equations are given by:

$$\overline{u'u'} = A_1 k + A_2 \frac{k}{\epsilon}(\overline{u'w'}W_{,x} - \overline{v'w'}W_{,y}) - 2c_\mu \frac{k^2}{\epsilon} U_{,x} + \frac{c_3 f_2}{c_1}\overline{v'v'}, \tag{30}$$

$$\overline{v'v'} = A_3 k + A_4 \frac{k}{\epsilon}(\overline{v'w'}W_{,y} - \overline{u'w'}W_{,x}) - 2c_\mu \frac{k^2}{\epsilon} V_{,y}, \tag{31}$$

$$\overline{u'v'} = A_5 \frac{k}{\epsilon}(\overline{v'w'}W_{,x} + \overline{u'w'}W_{,y}) - c_\mu \frac{k^2}{\epsilon}(U_{,y} + V_{,x}), \tag{32}$$

where

$$A_1 = \frac{2}{3}\left(\alpha - \frac{\beta}{2} + c_1 - 1\right)\left(\frac{1}{c_1}\right), \tag{33}$$

$$A_3 = \frac{2}{3}\left(\alpha - \frac{\beta}{2} + c_1 - 1\right)\left(\frac{1}{c_1 + 2c_3 f_2}\right), \tag{34}$$

$$A_2 = \frac{\beta}{c_1}, \tag{35}$$

$$A_4 = \frac{\beta}{c_1 + 2c_3 f_2}, \tag{36}$$

$$A_5 = \frac{\beta}{c_1 + (3/2)c_3 f_2}. \tag{37}$$

$k$ and $\epsilon$ in the above algebraic stresses are given by the following transport equations:

$$\mathbf{V}\cdot\nabla k = \left(\frac{\nu_{tx}}{\sigma_k} k_{,x}\right)_{,x} + \left(\frac{\nu_{ty}}{\sigma_k} k_{,y}\right)_{,y} + P_k - \epsilon, \tag{38}$$

$$\mathbf{V}\cdot\nabla \epsilon = \left(\frac{\nu_{tx}}{\sigma_\epsilon} \epsilon_{,x}\right)_{,x} + \left(\frac{\nu_{ty}}{\sigma_\epsilon} \epsilon_{,y}\right)_{,y} + c_{1\epsilon}\frac{\epsilon}{k}(P_k - c_{2\epsilon}\epsilon). \tag{39}$$

Table 2
Empirical functions in the Reynolds stresses

| $c_1$ | $c_3$ | $c_\mu$ | $\alpha$ | $\beta$ | $\gamma$ |
|---|---|---|---|---|---|
| $1.5 - 0.5f_1$ | 0.1 | 0.09 | $0.7636 - 0.06f_1$ | $0.1091 + 0.06f_1$ | 0.182 |

Table 3
Empirical constants in the ASM model

| $\sigma_k$ | $\sigma_\epsilon$ | $c_{1\epsilon}$ | $c_{2\epsilon}$ |
|---|---|---|---|
| 1.225 | 1.225 | 1.44 | 1.92 |

Here $P_k$ is the production rate of $k$ given by

$$P_k = -\overline{u'w'}W_{,x} - \overline{v'w'}W_{,y} = v_{tx}W_{,x}^2 + v_{ty}W_{,y}^2, \tag{40}$$

where gradients of secondary velocities are neglected. The constants in these equations are presented in Table 3. Note that the Prandtl numbers are slightly changed from the standard values. Naot and Rodi (1982) reported that this was done to obtain a better agreement with the eddy viscosity distribution obtained from measurements in two-dimensional closed channel flow.

### 2.4. Boundary conditions

Linear waves are assumed and boundary conditions for the wave field are prescribed at the mean interface:

$$\eta_{,t} + \widehat{W}\eta_{,z} = \tilde{v}, \quad y = H_{\mathrm{L}}, \tag{41}$$

$$\tilde{p} - \rho g\eta = 0, \quad y = H_{\mathrm{L}}, \tag{42}$$

$$\tilde{v} = 0, \quad y = 0. \tag{43}$$

These conditions entail the following boundary conditions for the potential fulfilment of the Rayleigh stability equation:

$$ak_{\mathrm{w}}(\widehat{W} - c) = \phi, \quad y = H_{\mathrm{L}}, \tag{44}$$

$$(\widehat{W} - c)\phi_{,y} - \phi\widehat{W}_{,y} - gak_{\mathrm{w}} = 0, \quad y = H_{\mathrm{L}}, \tag{45}$$

$$\phi = 0, \quad y = 0. \tag{46}$$

In solving the equation set, a long section of the duct is considered. A unidirectional uniform mean velocity field as well as a uniform turbulent field are specified as inlet conditions. The length of the duct is adjusted entailing a fully developed flow field at the outlet of the duct. Symmetry conditions are applied for the mean flow field at the middle of the duct $x = 0$. At the bottom and lateral walls, the wall shear stress $\tau_{\mathrm{w}}$ is found from inverting the logarithmic wall function for the tangential velocity component $U_{\mathrm{T}} = u_\tau \ln(Ey^+)/\kappa$, where $u_\tau = \sqrt{\tau_{\mathrm{w}}/\rho}$ is the friction velocity, $y^+ = yu_\tau/v$ is a dimensionless wall distance, $y$ is the distance from the wall, $\kappa = 0.42$ and $E = 9.0$. The wall shear stress (decomposed into the Cartesian directions) becomes the boundary condition for the velocity components parallel to the walls. The velocity component normal to the walls is set to zero. $k$ and $\epsilon$ are specified in the logarithmic wall layer by $k = u_\tau^2/\sqrt{c_\mu}$ and $\epsilon = u_\tau^3/(\kappa y)$. At

Table 4
Other model parameters

| | | | |
|---|---|---|---|
| $H_L = 0.0315$ m | $L_W = 0.1$ m | $\tau_i(0) = 0.256$ N/m$^2$ | $W_B = 0.476$ m/s |

the mean interface, a zero stress condition $U_{,y} = 0$ applies for the $U$ velocity component. For the $V$ velocity component a zero mean momentum flux normal to the mean interface is specified. The boundary condition for the $W$ velocity component at the mean interface is prescribed by the interfacial shear stress $\tau_i(x)$ condition

$$\tau_i(x) = \tau_i(0)\left(\frac{L_W - x}{L_W}\right)^{1/4}, \quad y = H_L, \tag{47}$$

previously used by Nordsveen (1995). The value $\tau_i(0)$ is taken from experiments (Table 4). The boundary condition (47) models the decrease in the interfacial shear stress towards the lateral walls. The interfacial boundary conditions used for $k$ and $\epsilon$ are

$$k_{,y} = 0, \quad y = H_L, \tag{48}$$

$$\epsilon = k^{3/2}/(0.18H_L), \quad y = H_L. \tag{49}$$

These interfacial conditions for $k$ and $\epsilon$ were used by Celik and Rodi (1984) for turbulent open channel flow, and the boundary condition for $\epsilon$ was chosen to obtain the correct decrease in eddy viscosity towards the interface. A zero gradient condition for $\epsilon$ together with the $k-\epsilon$ turbulence model used here was found to give an erroneous maximum eddy viscosity at the interface.

## 3. Numerical method

The CFD code PHOENICS (Roston and Spalding, 1987) was adjusted to solve the models outlined above. The model for the wave field was coded and the wave field–mean field interaction terms were given as sources in the mean momentum equation. The cross-section Reynolds stresses contain additional terms to the standard eddy viscosity terms in the PHOENICS code. These additional terms were implemented as source terms. Also the eddy viscosity in the axial momentum equation, the $k$-equation and the $\epsilon$ equation have been modified. A control volume method with a Cartesian, staggered grid is used. The resulting finite difference equations are solved sequentially in an efficient forward-marching solution procedure. That is, the equations are parabolized in the axial direction and two-dimensional equation systems are solved with the SIMPLE algorithm (Patankar, 1980), starting at the inlet of the duct, marching downstream until a fully developed state is obtained. First a solution applying the standard $k-\epsilon$ model was obtained. This flow field was then given as inlet condition in a subsequent simulation with the ASM model. For the open-channel flow simulations, some convergence problems were experienced. However, by applying strong underrelaxation for the turbulence sources for secondary velocities, a stable solution was reached.

## 4. Predictions

### 4.1. Turbulence-induced secondary flows

The implementation of the ASM turbulence model has been validated against closed-duct experiments by Po (1975), Lund (1977) and Gessner (1980) (PLG) and open channel flow experiments by Nezu and Rodi (1985).

PLG conducted experiments in a 22 m long square duct with 0.2554 m between opposite walls. They measured the mean velocities and Reynolds stresses at different positions along the duct for different Reynolds numbers. Predictions with the implemented model are compared with the measurements at the last position along the duct where the flow field was reported to be fully developed. The Reynolds number based on the bulk velocity $W_B$ and the hydraulic diameter $D_H$ was 250 000. In Fig. 3 axial and secondary velocities along wall and corner bisectors are presented. There is excellent agreement between model predictions and the experiments for the axial velocity. For the secondary velocities, there are small differences between the predictions and the experiments. Three non-uniform grids $20 \times 20$, $30 \times 30$ and $40 \times 40$ were applied and small differences

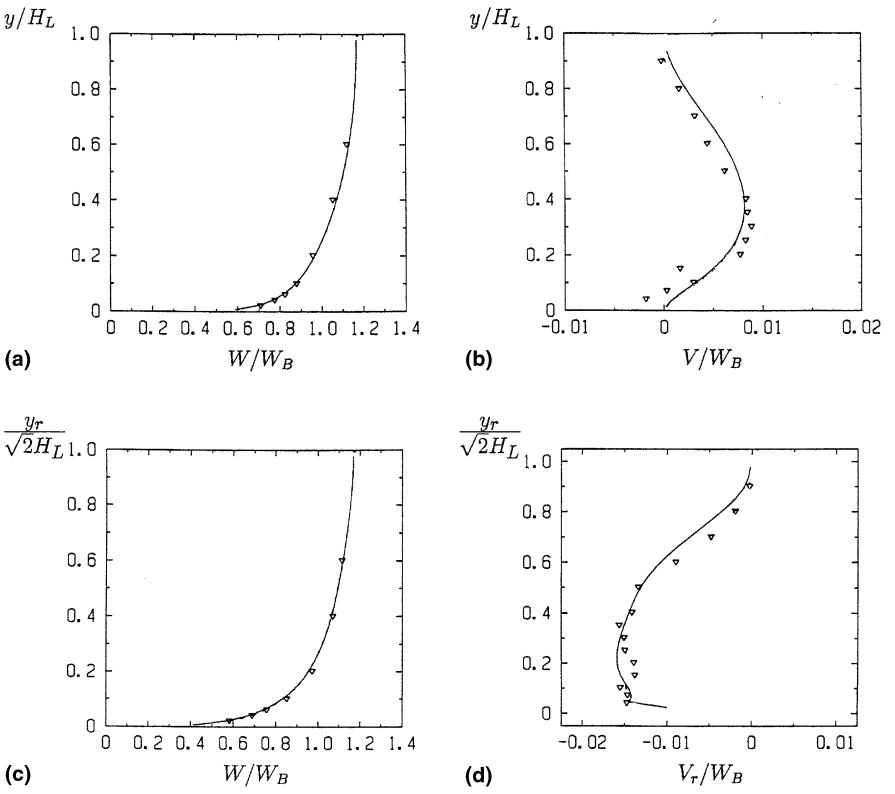


Fig. 3. (a) Axial velocity at wall bisector. (b) Secondary velocity at wall bisector. (c) Axial velocity at corner bisector. (d) Secondary velocity at corner bisector. The lines are predictions and triangles are experiments of PLG.

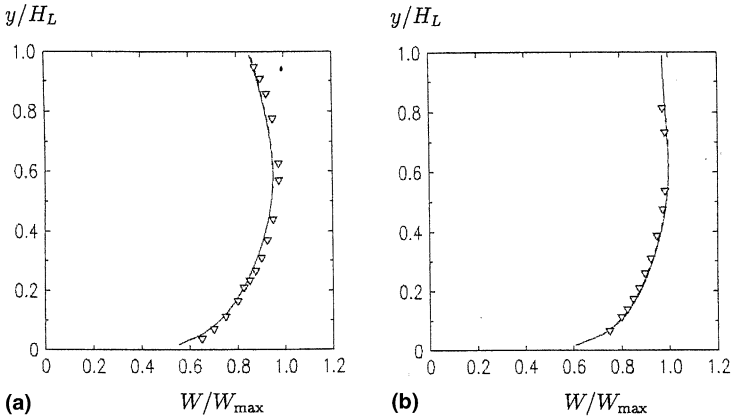


Fig. 4. Mean axial velocity. (a) Midway between the wall bisector and the lateral wall. (b) At the wall bisector. Grid $30 \times 30$. $\nabla$ – Exp. of Nezu and Rodi (1985). Solid line – ASM-model.

only were observed for the two finest grids. The predictions presented here were obtained on the finest grid.

Nezu and Rodi (1985) performed an experimental study of secondary currents in open channel flow with a free surface for several aspect ratios $2L_W/H_L$ ($2L_W$ is the channel width and $H_L$ is the liquid height). Predictions with the presented ASM model are compared with their results for a case with aspect ratio $2L_W/H_L = 2$, $H_L = 0.1$ m and bulk velocity $W_B = 0.5$ m/s. The axial velocities are compared in Fig. 4 and the secondary velocity fields in a quadrant of the cross-section are compared in Fig. 5. The correspondence between simulations and measurements is good. The predictions were obtained with a $30 \times 30$ grid, which gave a (nearly) grid independent solution for this case.

### 4.2. Wavy stratified flow in a wide duct

Predictions with the developed model have been compared with Suzanne's experiment C400 (1985) conducted in a 0.2 m wide duct with a 0.1° downward slope. For this case, Suzanne observed a regular two-dimensional wave field with a varying amplitude across the width of the duct. In this work, a constant wave amplitude of 0.0012 m has been used. This is less than the maximum amplitude close to the lateral walls and larger than the minimum amplitude in the center of the duct as reported by Suzanne. Values of the flow parameters are given in Table 5. $W_B$, $k_B$ and $\epsilon_B$ are the boundary conditions applied at the inlet of the duct. Predictions of secondary flow fields over half the cross-section are shown in Fig. 6. It is seen that when only turbulence-induced secondary flows are considered, Fig. 6(a), very small secondary flows are seen in the central part of the duct. For this particular simulation, the shear stress at the interface was set to zero due to problems in obtaining a stable and reliable solution with a non-zero interfacial shear stress. The downward flow does not occur in the center of the duct, and this seemed to cause the problem. The ASM model was originally developed for open channel flow with zero shear stress and a prediction with zero shear stress is therefore shown. In Fig. 6(b), only wave-induced secondary flows are

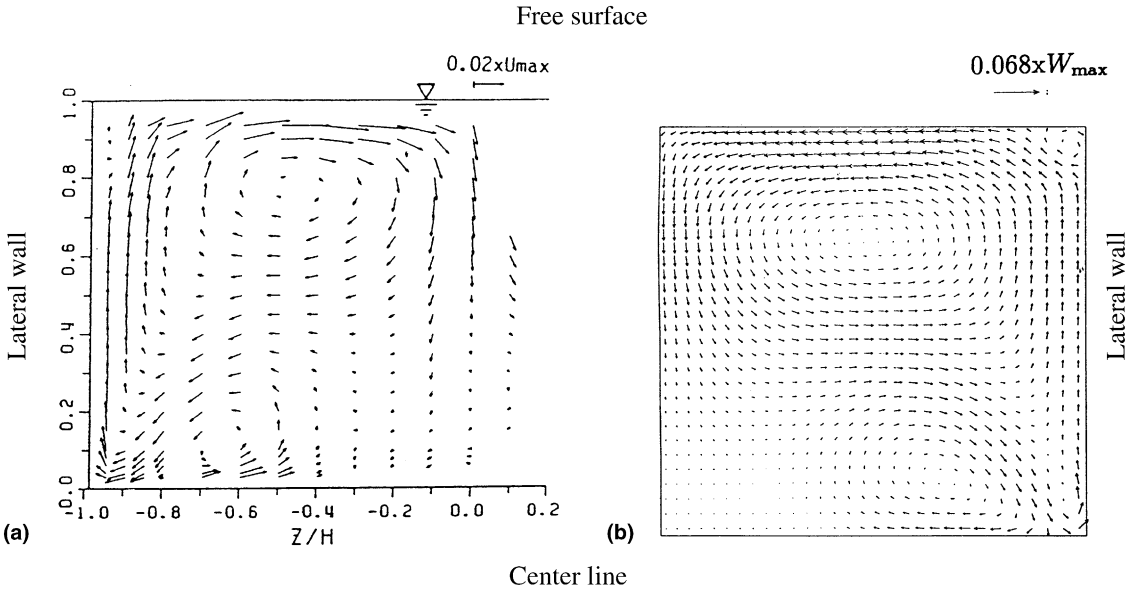


Fig. 5. Secondary velocity field over half the cross-section. (a) Experiments of Nezu and Rodi (1985), left side of duct. (b) ASM-model, right side of duct.

Table 5
Values describing the case which is simulated

| Geometry | Fluid properties | Boundary conditions | Wave field parameters |
|---|---|---|---|
| $H_L = 0.0315$ m | $\rho = 1000$ kg/m$^3$ | $W_B = 0.476$ m/s | $a = 0.0012$ m |
| $L_W = 0.1$ m | $\nu = 1.0 \times 10^{-6}$ m$^2$/s | $k_B = 0.05$ (m/s)$^2$ | $k_w = 64.77$ m$^{-1}$ |
| $\gamma = 0.1°$ | | $\epsilon_B = 0.05$ m$^2$/s$^3$ | |
| | | $\tau_i(0) = 0.2675$ kg/(ms$^2$) | |

considered, while in Fig. 6(c) both effects are included. For these two latter cases, the non-zero shear stress boundary condition given by Eq. (47) was applied. That is, when combining the two mechanisms no convergence problems were experienced.

In Fig. 7 vertical secondary velocities at three different verticals (13, 60 and 93 mm from the middle of duct) are presented. In Fig. 7(a–c) only turbulence-induced secondary currents were considered. The predicted vertical velocity near the middle of the duct is close to zero, in disagreement with Suzanne's measurements. Close to the lateral walls, the predicted secondary velocities have the correct order of magnitude. However, near the bottom of the duct, negative velocities are predicted while the measured ones are close to zero. In Fig. 7(d–f) only wave-induced secondary currents were modelled. Larger vertical velocities near the central part of the duct are predicted, but they are still less than the measured ones. Near the lateral walls, secondary velocities with the right order of magnitude are predicted, but with larger values than measured near the bottom and smaller values near the interface. In Fig. 7(g–i) both wave- and turbulence-induced secondary currents were modelled. A significant improvement is observed with good

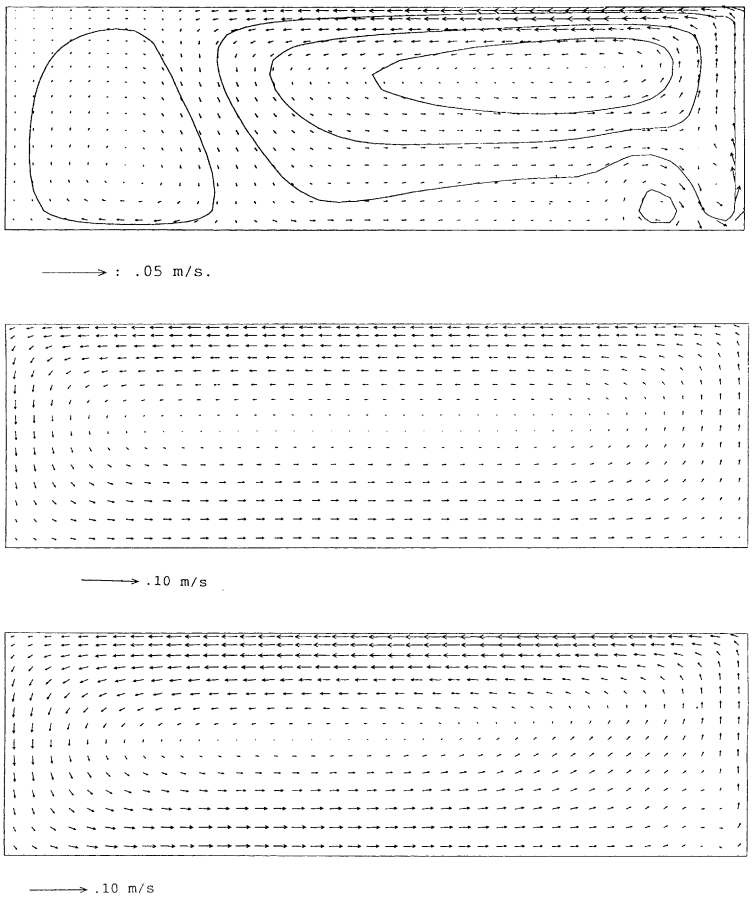


Fig. 6. (a) The ASM simulation – turbulence-induced secondary velocity field. (b) The GLM simulation – wave-induced secondary velocity field. (c) The ASM–GLM simulations – wave- and turbulent-induced secondary velocity field.

agreement both in the central part of the duct and near the lateral walls. Near the lateral walls, the two effects almost cancel each other close to the bottom of the duct, while they enhance each other towards the interface.

In Fig. 8 the axial velocities at three different verticals (0, 60 and 93 mm from the middle of duct) are presented. Again it is seen that the best agreement with measurements is obtained when both turbulence- and wave-induced secondary currents are taken into account. However, there is an overprediction in the center of the duct and an underprediction at the lateral walls.

### *4.3. Wavy stratified flow in a duct with aspects ratio 2*

In the comparison between wave- and turbulence-induced secondary flow for Suzanne's experiment C400 (1985), it was seen that the wave field model was the larger contributor to the secondary currents. These results were obtained for a wide duct.

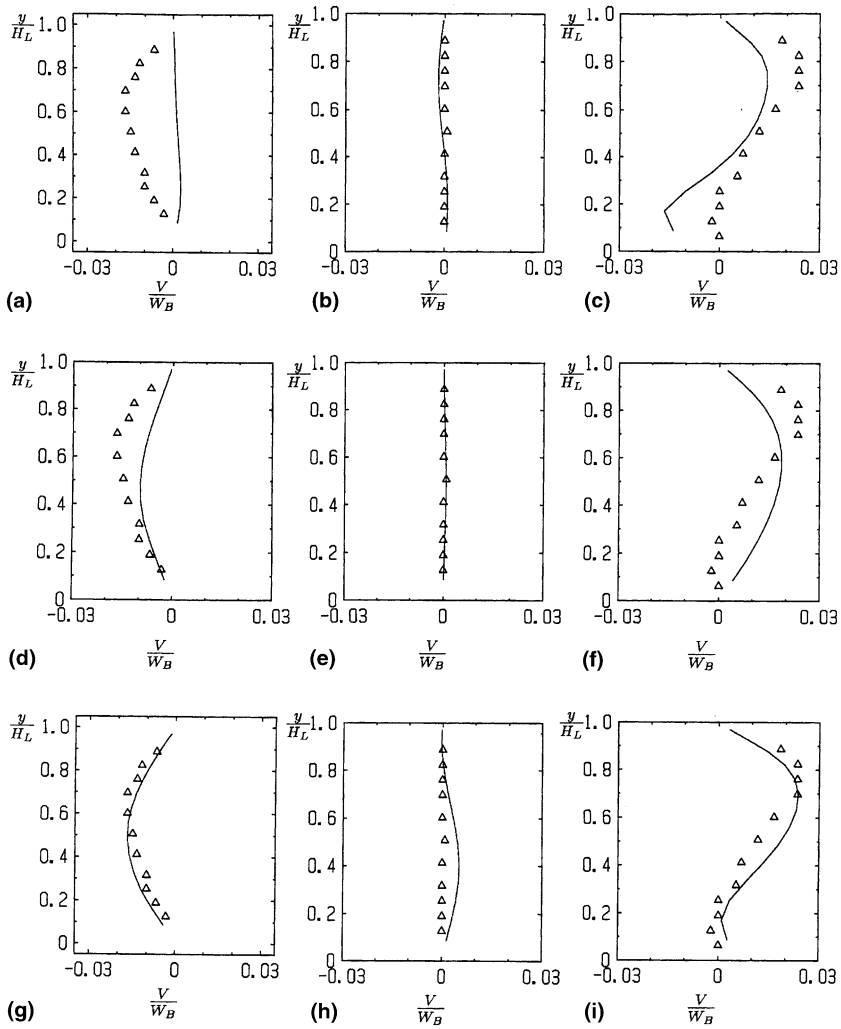


Fig. 7. Vertical secondary velocities (solid line – predictions, triangles – experiments of Suzanne (1985)). (a) ASM model at 13 mm. (b) ASM model at 60 mm. (c) ASM model at 93 mm. (d) GLM model at 13 mm. (e) GLM model at 60 mm. (f) GLM model at 93 mm. (g) ASM + GLM models at 13 mm. (h) ASM + GLM models at 60 mm. (i) ASM + GLM models at 93 mm.

Here a comparison of wave- and turbulence-induced secondary velocities for a more narrow duct with the aspect ratio $2L_W/H_L = 2$ is performed. Except for the change of $L_W$ to 3.15 cm, all other parameters are taken identical to the C400 case (see Table 5). The shear stress boundary condition given by Eq. (47) was applied.

In Fig. 9 the horizontal secondary velocity $U$ is plotted at two verticals. It is seen that the two effects induce secondary currents of the same magnitude. By combining the two effects about a 50% increase of the secondary velocities is obtained.

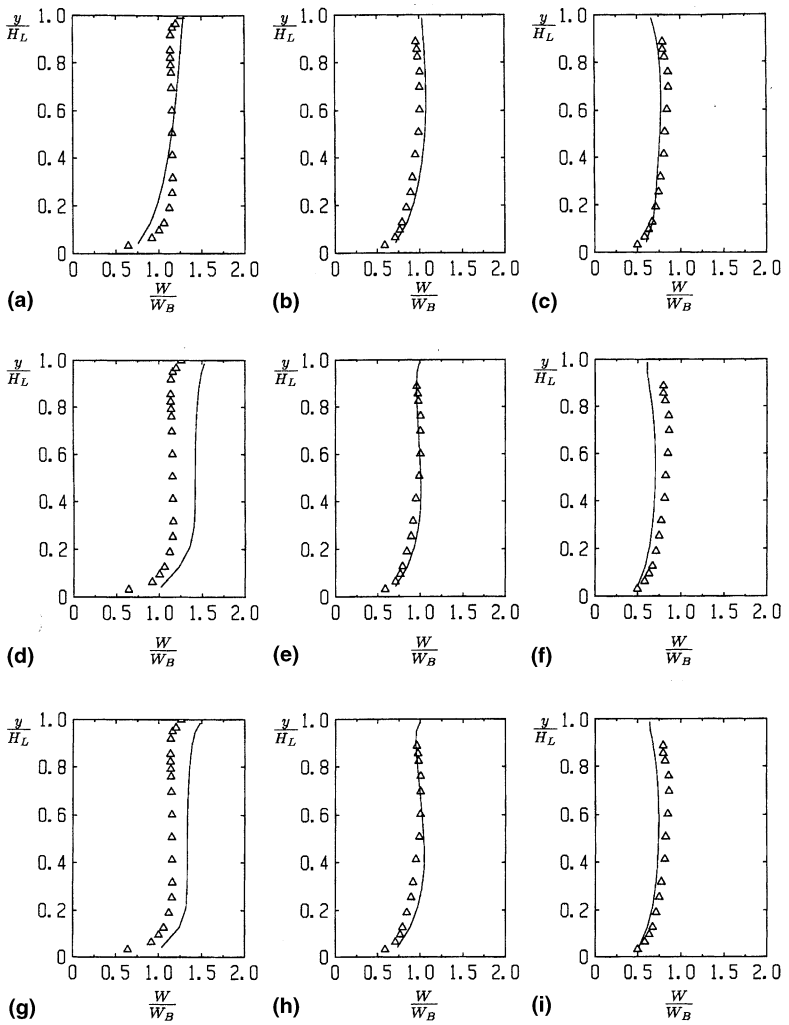


Fig. 8. Axial velocities, solid line – predictions, triangles – experiments of Suzanne (1985). (a) ASM model at 0 mm. (b) ASM model at 60 mm. (c) ASM model at 93 mm. (d) GLM model at 0 mm. (e) GLM model at 60 mm. (f) GLM model at 93 mm. (g) ASM + GLM models at 0 mm. (h) ASM + GLM models at 60 mm. (i) ASM + GLM models at 93 mm.

In Fig. 10 vorticity sources over half the cross-section due to the wave field and the turbulent field are presented. It is seen that the maximum vorticity source due to the turbulent field is larger than the maximum vorticity source due to the wave field. However, the turbulent-induced source is mainly localized to the wall–wall corner and the wall–interface intersection while the wave-induced source acts all along the interface. For this case the integrated effects for the two phenomena were similar.

The vorticity sources for the more narrow duct were quite similar to the ones predicted for Suzanne's case C400, but for the wide duct case the longer interface length entailed a larger integrated wave effect.

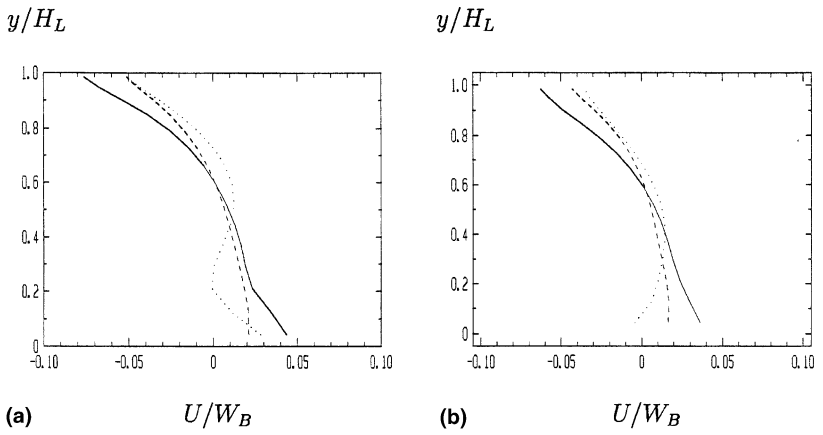


Fig. 9. Horizontal secondary velocity made dimensionless with the bulk velocity. (a) At the vertical line $x = L_W/3$. (b) At the vertical line $x = 2L_W/3$. Dotted line – the ASM simulation, dashed line – the GLM simulation, solid line – the ASM–GLM simulation.

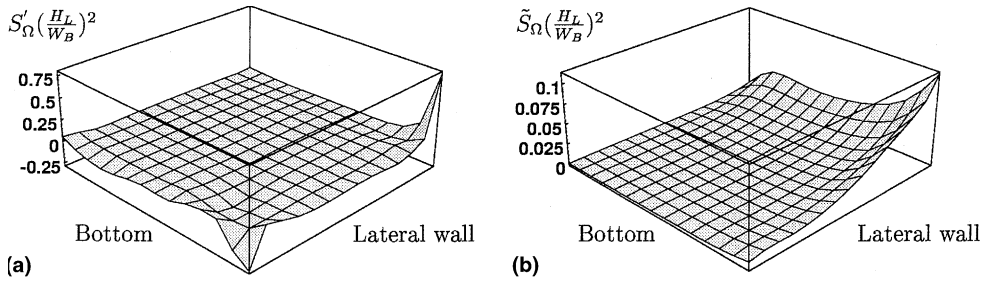


Fig. 10. Surface plots of vorticity sources over half the cross-section. The corner points out of the paper with the walls in front. The vorticity sources are made dimensionless with the square of the bulk velocity divided by the liquid height. (a) ASM model, (b) GLM model.

## 5. Conclusions

The objective of this work was to compare turbulence- and wave-induced secondary currents in the liquid phase in stratified duct flow. It was previously shown (Nordsveen and Bertelsen, 1997) that secondary velocities in the liquid phase may result from an interaction between wave pseudomomentum and mean axial velocity. The same wave field–mean field interactions have been applied in the present work.

Numerous experimental, theoretical and numerical studies have also addressed turbulence-induced secondary currents in ducts or pipes with non-circular cross-sections. These flows are induced by anisotropy in the turbulence. The ASM developed by Naot and Rodi (1982) was tailored to handle open channel flow and this model was implemented.

Turbulence- and wave-induced secondary flows have been compared for Suzanne's experiment C400 (1985) with stratified duct flow with a regular wave deformation of the interface caused by a concurrently flowing gas phase. Suzanne observed strong mean secondary flow, which formed a cellular structure with two rolls in the liquid phase and two rolls in the gas phase. The liquid was flowing up near the walls and down in the middle of the duct, while the gas was flowing up in the middle and down near the walls. For this case, the width of the duct was 20 cm and the liquid height was 3.15 cm (aspect ratio >6).

Using the ASM model without any wave field model, very weak secondary flows were predicted in the central part of the duct. The turbulence-induced secondary flow was mainly generated in the bottom wall–lateral wall corners and the lateral wall–interface intersections. It did not penetrate all the way into the central part of the duct. The computed strength of the secondary velocities in the corner regions was smaller than that reported by Suzanne (1985), but of the same order of magnitude.

When using a $k-\epsilon$ turbulence model (which does not generate secondary currents) and the GLM wave field model, secondary flow was induced all over the cross-section of the duct. In the central part of the duct, the predicted secondary velocities were still less than the measured ones. Near the lateral walls, secondary velocities with the right magnitude were predicted, but with larger values than those measured near the bottom and smaller values near the interface.

By applying the ASM turbulence model and the GLM wave field model, both wave- and turbulence-induced secondary currents were modelled. A significant improvement was observed with good agreement both in the central part of the duct as well as near the lateral walls. Near the lateral walls the two effects almost cancelled each other close to the bottom of the duct, while they enhanced each other towards the interface.

For Suzanne's experiment C400 (1985), the wave-induced secondary flow was larger than that induced by the turbulence. The maximum vorticity source due to the turbulent field was larger than the maximum vorticity source due to the wave field. However, the turbulent-induced source is localized to the wall–wall corners and the wall–interface intersections. The wave-induced source acts all along the interface and with a duct width of 20 cm and liquid height of about 3 cm, the integrated effect of the wave field became larger than that of the turbulent field with respect to inducing secondary velocities.

Wave- and turbulence-induced secondary currents were also compared for a duct flow with the liquid width-to-liquid height aspect ratio equal to 2. The same flow parameters as in Suzanne's experiment C400 were used, except that the width of the duct was reduced to twice the liquid height. For this case, the wave and turbulence models were of equal importance for generating secondary currents. Both models predicted a strong secondary flow all over the cross-section. By combining the two effects, the strength of the predicted secondary velocities was increased by about 50%.

## Appendix A. Near surface correction in the ASM model

Close to walls or interfaces, near-surface corrections have been introduced to model the damping of the normal stresses perpendicular to the surface and, by continuity, the augmentation of the normal stresses parallel to the surface.

### A.1. Wall proximity term – function $f_1$

Launder et al. (1975) modelled the effect of walls by specifying the empirical constants in the pressure–strain terms to be functions of the distance from the surface. $f_1$ is a function of the dimensionless distance from the surface and is modelled as

$$f_1 = l^2\left[\frac{1}{y^2}\right], \tag{A.1}$$

where $l$ is the turbulent length scale defined by

$$l = \frac{c_\mu^{3/4}}{\kappa}\frac{k^{3/2}}{\epsilon} = \frac{c_D}{\kappa}\frac{k^{3/2}}{\epsilon} \tag{A.2}$$

with $\kappa = 0.435$ and $c_D = 0.1643$. With this definition of $l$, $f_1$ takes the value of unity in the log-layer near a plane wall. $[1/y^2]$ is the average reciprocal of the square of the distance from the surrounding walls and is defined as

$$\left[\frac{1}{y^2}\right] = \frac{2}{\pi}\int_0^{2\pi}\frac{1}{s^2}\,\mathrm{d}\Phi. \tag{A.3}$$

$s$ and $\Phi$ are defined in Fig. 11.

For a rectangular duct (four walls), $[1/y^2]$ is given by

$$\left[\frac{1}{y^2}\right] = \frac{1}{\pi}\left\{\frac{1}{x_1y_1}+\frac{1}{x_1y_2}+\frac{1}{x_2y_1}+\frac{1}{x_2y_2} + \frac{1}{y_1^2}\left[\arcsin\left(\frac{x_1}{(x_1^2+y_1^2)^{1/2}}\right)+\arcsin\left(\frac{x_2}{(x_2^2+y_1^2)^{1/2}}\right)\right]\right.$$

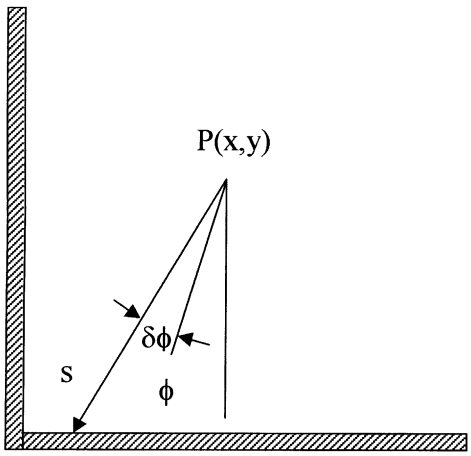


Fig. 11. Notation for calculating the average distance of point $P(x,y)$ from surface (from Naot and Rodi (1982)).

$$+\frac{1}{x_1^2}\left[\arcsin\left(\frac{y_1}{(x_1^2+y_1^2)^{1/2}}\right)+\arcsin\left(\frac{y_2}{(x_1^2+y_2^2)^{1/2}}\right)\right]$$
$$+\frac{1}{y_2^2}\left[\arcsin\left(\frac{x_2}{(x_2^2+y_1^2)^{1/2}}\right)+\arcsin\left(\frac{x_1}{(x_1^2+y_2^2)^{1/2}}\right)\right]$$
$$+\frac{1}{x_2^2}\left[\arcsin\left(\frac{y_1}{(x_2^2+y_1^2)^{1/2}}\right)+\arcsin\left(\frac{y_2}{(x_2^2+y_2^2)^{1/2}}\right)\right]\Bigg\}, \tag{A.4}$$

where $x_1$ and $x_2$ are the distances from two opposite walls, and $y_1$ and $y_2$ are the distances from the two other walls.

For an open channel (three walls), $[1/y^2]$ is given by

$$\left[\frac{1}{y^2}\right]=\frac{1}{\pi}\Bigg\{\frac{1}{x_1y_1}+\frac{1}{x_2y_1}+\frac{y_2}{x_1(x_1^2+y_2^2)}+\frac{y_2}{x_2(x_2^2+y_2^2)}$$
$$+\frac{1}{y_1^2}\left[\arcsin\left(\frac{x_1}{(x_1^2+y_1^2)^{1/2}}\right)+\arcsin\left(\frac{x_2}{(x_2^2+y_1^2)^{1/2}}\right)\right]$$
$$+\frac{1}{x_1^2}\left[\arcsin\left(\frac{y_1}{(x_1^2+y_1^2)^{1/2}}\right)+\arcsin\left(\frac{y_2}{(x_1^2+y_2^2)^{1/2}}\right)\right]$$
$$+\frac{1}{x_2^2}\left[\arcsin\left(\frac{y_1}{(x_2^2+y_1^2)^{1/2}}\right)+\arcsin\left(\frac{y_2}{(x_2^2+y_2^2)^{1/2}}\right)\right]\Bigg\}, \tag{A.5}$$

where $x_1$ and $x_2$ are the distances from the lateral walls, $y_1$ is the distance from the bottom wall and $y_2$ is the distance from the interface.

### A.2. Free surface proximity term – function $f_2$

Naot and Rodi (1982) pointed out that the surface-proximity correction of Launder et al. (1975) does not produce the correct anisotropy in the Reynolds stresses close to a free surface, where the mean velocity gradients become small. For open-channel flow predictions, they therefore used the Launder, Reece and Rodi surface-proximity model for three solid walls and the Shir (1973) surface-proximity model for a free surface. This surface-proximity correction, which models anisotropy in weak shear flow better, is given by

$$\phi_{ij}^s=c_3\frac{\epsilon}{k}\left(\overline{v_k'v_m'}\mathbf{n}_k\mathbf{n}_m\delta_{ij}-\frac{3}{2}\overline{v_k'v_i'}\mathbf{n}_k\mathbf{n}_j-\frac{3}{2}\overline{v_k'v_j'}\mathbf{n}_k\mathbf{n}_i\right)f_2, \tag{A.6}$$

where $c_3=0.1$, $i$, $j$, $k$, $m$, $n=1$, 2, 3 and $\mathbf{n}$ is a unit vector normal to the free surface.

$f_2$ is a function of the distance from the free surface given by

$$f_2=\left(\frac{l}{\left[1/y_s^2\right]^{-1/2}+c_f l}\right)^2 \tag{A.7}$$

with $c_f = 0.16$. $[1/y_s^2]$ is the average reciprocal of the square of the distance from the free surface given by

$$\left[\frac{1}{y_s^2}\right] = \frac{1}{\pi y_2^2}\left(\frac{x_2 y_2}{x_2^2+y_2^2} + \frac{x_1 y_2}{x_1^2+y_2^2} + \arcsin\left(\frac{x_2}{(x_2^2+y_2^2)^{1/2}}\right) + \arcsin\left(\frac{x_1}{(x_1^2+y_2^2)^{1/2}}\right)\right), \qquad (A.8)$$

where $x_1$ and $x_2$ are the distances from the lateral walls and $y_2$ is the distance from the free surface.

## References


Akai, M., Inoue, A., Aoki, S., 1977. Structure of a co-current stratified two-phase flow with wavy interphase. Theor. Appl. Mech. 25, 445–455.

Andrews, D.G., McIntyre, M.E., 1978. An exact theory of nonlinear waves on a Lagrangian-mean flow. J. Fluid Mech. 89, 609–646.

Benkirane, R., Line, A., Masbernat, L., 1990. Modelling of wavy stratified flow in a rectangular channel. In ICHMT International Seminar on Phase-Interface Phenomena in Multiphase Flow, Dubrovnik, 14–18 May 1990.

Brundrett, E., Baines, W.D., 1964. Production and diffusion of vorticity in duct flow. J. Fluid Mech. 19, 375–394.

Celik, I., Rodi, W., 1984. Simulation of free-surface effects in turbulent channel-flows. Phys. Chem. Hydrodynamics 5, 217–227.

Craik, A.D.D., Leibovich, S., 1976. A rational model for Langmuir circulations. J. Fluid. Mech. 73, 401–426.

Craik, A.D.D., 1977. The generation of Langmuir circulations by an instability mechanism. J. Fluid Mech. 81, 209–223.

Craik, A.D.D., 1982. The generalized Lagrangian-mean equations and hydrodynamic stability. J. Fluid Mech. 125, 27–35.

Einstein, H.A., Li, H., 1958. Secondary currents in straight channels. Trans. Am. Geophys. Union 39, 1085–1088.

Gessner, F.B., 1980. Final report: Corner Flow Data Evaluation, Department of Mechanical Engineering, University of Washington.

Hanratty, T.J., Engen, 1957. Interaction between a turbulent air stream and a moving water surface. AICHE J. 3, 299–304.

Huser, A., 1992. Direct numerical simulation of turbulent flow in a square duct. Ph.D. Thesis, Department of Aerospace Engineering Sciences, University of Colorado.

Langmuir, I., 1938. Surface motion of water induced by wind. Science 87, 119–123.

Leibovich, S., 1977. Convective instability of stably stratified water on the ocean. J. Fluid Mech. 82, 561–585.

Leibovich, S., 1983. The form and dynamics of Langmuir circulations. Ann. Rev. Fluid Mech. 15, 391–427.

Launder, B.E., Reece, G.J., Rodi, W., 1975. Progress in the development of a Reynolds-stress turbulence closure. J. Fluid Mech. 86, 491–511.

Line, A., Masbernat, L., Soualmia, A., 1996. Interfacial interactions and secondary flows in stratified two-phase flow. Chem. Eng. Commun. 141–142, 303–329.

Lund, E.G., 1977. Mean flow and turbulence characteristics in the near corner region of a square duct. MS Thesis, Department of Mechanical Engineering, University of Washington.

Magnaudet, J., 1989. Interactions interfaciales en écoulement à phases séparées. Thèse de Doctorat, Institut National Polytechnique de Toulouse.

Naot, D., Rodi, W., 1982. Calculation of secondary currents in channel flow. J. Hydraulics Division ASCE 108, 948–968.

Nezu, I., Rodi, W., 1985. Experimental study on secondary currents in open channel flow. in: Proceedings of the 21st IAHR Congress. Melbourne, vol. 2, pp. 115–119.

Nikuradse, J., 1926. Geschwindigkeitsverteilung in turbulenten Strömungen. Z. Ver. Dtsch Ing. 70, 1229–1230.

Nordsveen, M., 1995. Modelling of wave and turbulence induced secondary currents in stratified duct flow. Thesis for Doctor Scientiarium, Mechanics Division, Department of Mathematics, University of Oslo.

Nordsveen, M., Bertelsen, A.F., 1996. Waves and secondary flows in stratified gas/liquid duct flow. Waves and Nonlinear Processes in Hydrodynamics. Kluwer Academic Publishers, Dordrecht.

Nordsveen, M., Bertelsen, A.F., 1997. Wave induced secondary motions in stratified duct flow. J. Multiphase Flow 23, 503–522.

Patankar, S.V., 1980. Numerical Heat Transfer and Fluid Flow. Hemisphere, Washington, DC.

Perkins, H.J., 1970. The formation of streamwise vorticity in turbulent flow. J. Fluid Mech. 44, 721–740.

Po, J.K., 1975. Developing turbulent flow in the entrance region of a square duct. MS Thesis, Department of Mechanical Engineering, University of Washington.

Prandtl, L., 1926. Ueber die ausgebildete Turbulence. Verh. 2nd. Int. Kong. Tech. Mech., Zuerich.

Reynolds, W.C., Hussain, A.K.M.F., 1972. The mechanics of an organized wave in turbulent shear flow. Part 3. Theoretical models and comparisons with experiments. J. Fluid Mech. 54, 263–288.

Rodi, W., 1980. Turbulence Models and Their Application in Hydraulics. IAHR Book Publication, Delft, Netherlands.

Roston, H.I., Spalding, D.B., 1987. The phoenics reference manual, CHAM TR/200.

Shir, C.C., 1973. A preliminary numerical study of atmospheric turbulent flows in the idealized planetary boundary layer. J. Atmos. Sci. 30, 1327–1339.

Strand, Ø., 1993. An experimental investigation of stratified two-phase flow in horizontal pipes. Thesis for Doctor Scientiarium, Mechanics Division, Department of Mathematics, University of Oslo.

Suzanne, C., 1985. Structure de l'ecoulement stratifie de gaz et de liquide en canal rectangulaire. These de Docteur es Sciences, Institut National Polytechnique de Toulouse.